iScience

CellPress

Article

Unveiling Property of Hydrolysis-Derived $DMAPbI_3$ for Perovskite Devices: Composition Engineering, Defect Mitigation, and Stability Optimization

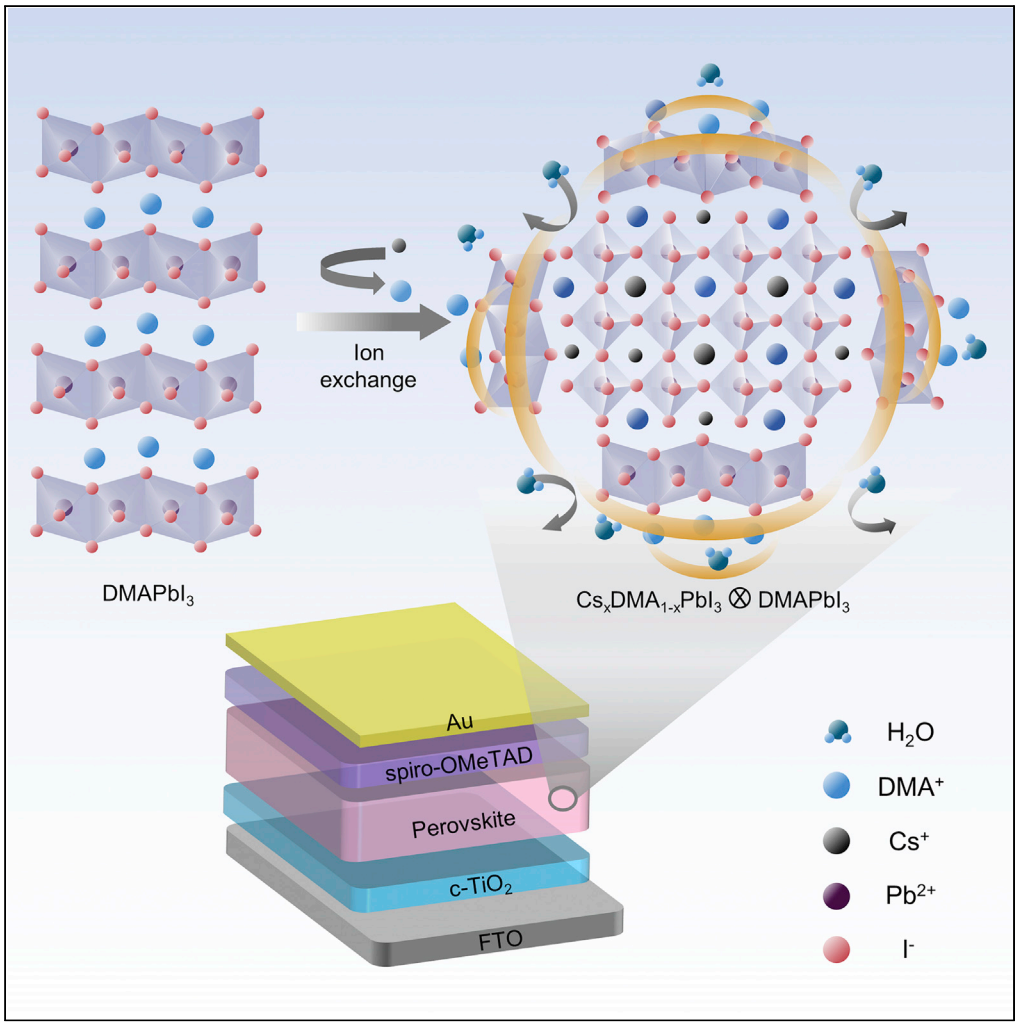

Yunhe Pei, Yang Liu, Faming Li, Sai Bai, Xian Jian, Mingzhen Liu

mingzhen.liu@uestc.edu.cn

HIGHLIGHTS

Dissolving PbI_2 and HI in DMF is confirmed not to produce the "mythical" $HPbI_3$

Detailed composition analyses show that $DMAPbI_3$ is the hydrolysis product instead

Performance of devices can be optimized by tuning the CsI:$DMAPbI_3$ ratio

The $Cs_xDMA_{1-x}PbI_3$ films remain stable in air for more than 20 days

Pei et al., iScience *15*, 165–172
May 31, 2019
https://doi.org/10.1016/j.isci.2019.04.024

iScience

CellPress

Article

Unveiling Property of Hydrolysis-Derived $DMAPbI_3$ for Perovskite Devices: Composition Engineering, Defect Mitigation, and Stability Optimization

Yunhe Pei,[1,2,4] Yang Liu,[1,2,4] Faming Li,[1,2] Sai Bai,[3] Xian Jian,[1,2] and Mingzhen Liu[1,2,5,*]

SUMMARY

Additive engineering has become increasingly important for making high-quality perovskite solar cells (PSCs), with a recent example involving acid during fabrication of cesium-based perovskites. Lately, it has been suggested that this process would introduce dimethylammonium ($(CH_3)_2NH_2^+$, DMA^+) through hydrolysis of the organic solvent. However, material composition of the hydrolyzed product and its effect on the device performance remain to be understood. Here, we present an in-depth investigation of the hydrolysis-derived material (i.e., $DMAPbI_3$) and detailed analysis of its role in producing high-quality PSCs. By varying the ratio of $CsI/DMAPbI_3$ in the precursor, we achieve high-quality $Cs_xDMA_{1-x}PbI_3$ perovskite films with uniform morphology, low density of trap states, and good stability, leading to optimized power conversion efficiency up to 14.3%, with over 85% of the initial efficiency retained after ~20 days in air without encapsulation. Our findings offer new insights into producing high-quality Cs-based perovskite materials.

INTRODUCTION

As an emerging alternative light-harvesting material in solar cells, cesium (Cs)-based halide perovskites have recently attracted booming attention due to their excellent charge transport properties and thermal stability (Wang et al., 2018a, 2018b, 2018d; Li et al., 2018b). It has been demonstrated that α-$CsPbI_3$ (cubic phase) exhibits a band gap of ~1.73 eV, highly desirable for building top cells in tandem perovskite solar cells (PSCs). However, α-$CsPbI_3$ perovskite exhibits a tolerance factor of ~0.85, making the materials unstable at room temperature due to the easily spontaneous transformation to the photo-inactive δ phase (Hu et al., 2017; Lau et al., 2018), severely hampering its application toward high-performance PSCs. Among various approaches (Wang et al., 2017, 2018a, 2018b, 2018c, 2018d; Hu et al., 2017; Lau et al., 2018; Jena et al., 2018; Swarnkar et al., 2016; Sanehira et al., 2017; Zhang et al., 2017; Liao et al., 2017; Luo et al., 2016; Fu et al., 2017; Li et al., 2018a, 2018b), additive engineering, which involves careful selection and addition of components to the precursor solution, has been commonly employed for the perovskite deposition to achieve a better control of the crystallization process and the ensuing film quality (Sutherland, 2017). Optimization of the additive engineering has been demonstrated as an effective and facile route toward Cs-based photovoltaic devices with improved efficiency and stability and has become an emerging focus of PSC research.

As an exemplary case, adding hydriodic acid (HI) to the *N,N*-dimethylformamide (DMF) solution of lead iodide (PbI_2) and cesium iodide (CsI) has been demonstrated as a popular way to enhance the phase stability of the resultant Cs-based perovskite films (Eperon et al., 2015; Hu et al., 2017; Luo et al., 2016). However, the understanding of the detailed reaction mechanism and actual role of the additives has often remained elusive, which hinders further optimization of the fabrication process. For example, it has recently been suggested that the "mythical" hydrogen lead trihalide ($HPbI_3$, also known as $PbI_2 \cdot xHI$), the often-assumed reaction product of HI and PbI_2, does not actually exist (Ke et al., 2018). Instead, adding acid to DMF is known to generate a weak base dimethylamine (DMA) through hydrolysis (Noel et al., 2017; Sutherland, 2017; Daub and Hillebrecht, 2018), and with the presence of PbI_2 the actual final product is believed to be a compound of $DMAPbI_3$ (DMA^+ = dimethylammonium, $(CH_3)_2NH_2^+$). Despite the broad adoption of such reaction route in fabricating Cs-based perovskite materials, systematic investigation of $DMAPbI_3$ as the starting material and its effect on the performance of the resultant PSCs has been largely missing, breeding continued debates and confusion.

Here, we present a detailed characterization of the hydrolysis-derived $DMAPbI_3$ and its role in producing high-quality Cs-based perovskite films. We employed an extensive set of techniques to accomplish

[1]School of Materials and Energy, University of Electronic Science and Technology of China, Chengdu 611731, P. R. China

[2]Center for Applied Chemistry, University of Electronic Science and Technology of China, Chengdu 611731, P. R. China

[3]Department of Physics, Chemistry and Biology (IFM), Linköping University, Linköping 58183, Sweden

[4]These authors contributed equally

[5]Lead Contact

*Correspondence: mingzhen.liu@uestc.edu.cn

https://doi.org/10.1016/j.isci.2019.04.024

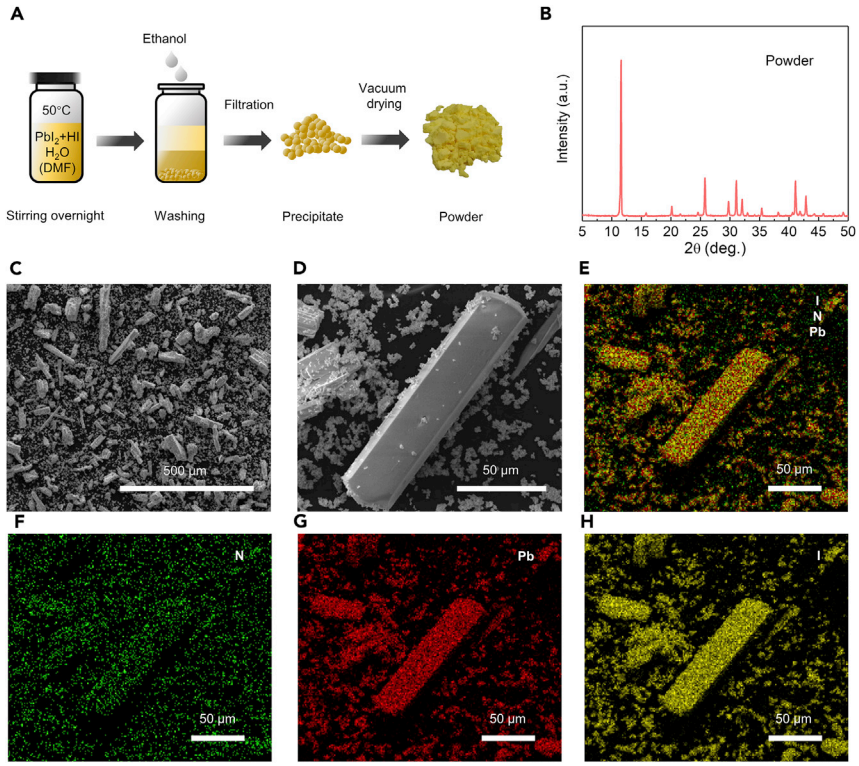

Figure 1. Synthesis and Characterization of the $DMAPbI_3$ Powder

(A) Schematic diagram for synthesizing $DMAPbI_3$ powder.

(B) XRD pattern of the $DMAPbI_3$ powder.

(C and D) SEM images of the $DMAPbI_3$ powder with different resolutions, See also Figure S1.

(E–H) Energy-dispersive spectrometric (EDS) mapping for N, Pb, and I elements in the $DMAPbI_3$ powder: EDS mapping of (E) N, Pb, and I elements overlay, (F) N element, (G) Pb element, and (H) I element distribution of the $DMAPbI_3$ powder.

in-depth analysis of the composition and properties of $DMAPbI_3$ as the starting material, including *in situ* thermogravimetry Fourier transform infrared spectroscopy (TG-FTIR) coupled analysis, nuclear magnetic resonance (NMR), and FTIR. We systematically tuned the $CsI/DMAPbI_3$ molar ratio in the precursor and investigated its effect on the film property of the perovskite material, including film morphology, defect states density, carrier lifetime, and material stability, among other PSC performance metrics. We achieve a power conversion efficiency (PCE) up to 14.3%, with over 85% of the initial efficiency retained after ~20 days in ambient condition without encapsulation. Our findings offer new insights into this important fabrication process, which can lead to better implementation and further optimization in producing high-quality Cs-based perovskite materials for solar cells with improved efficiency and stability.

RESULTS AND DISCUSSION

We synthesized the $DMAPbI_3$ powder following the commonly used method by reacting PbI_2 and HI in DMF (details in Methods section), which is used as the starting material for making the Cs-based perovskite films (Figure 1A). This method was once widely believed to produce the "mythical" $HPbI_3$ (Wang et al., 2015; Pang et al., 2016; Long et al., 2016), whereas a recent study challenged such claim and proposed that the product would be $DMAPbI_3$ (Ke et al., 2018; Daub and Hillebrecht, 2018), which is now confirmed, finally, by our detailed analysis as described below.

X-ray diffraction (XRD) patterns of the synthesized powder (Figure 1B) show peaks at 11.6°, 20.2°, 25.8°, 31.1°, 32.1°, 35.4°, 41.1°, and 42.8°, which can be well ascribed to $DMAPbI_3$ (Mancini et al., 2016; Ke et al., 2018). In addition, the scanning electron microscopic (SEM) images (Figures 1C and 1D) show that the powder particles have the shape of hexagonal rods (Figures 1D and S1), consistent with $DMAPbI_3$ crystals (Mancini et al., 2016; Ju et al., 2017). Furthermore, energy-dispersive spectrometric (EDS) mapping

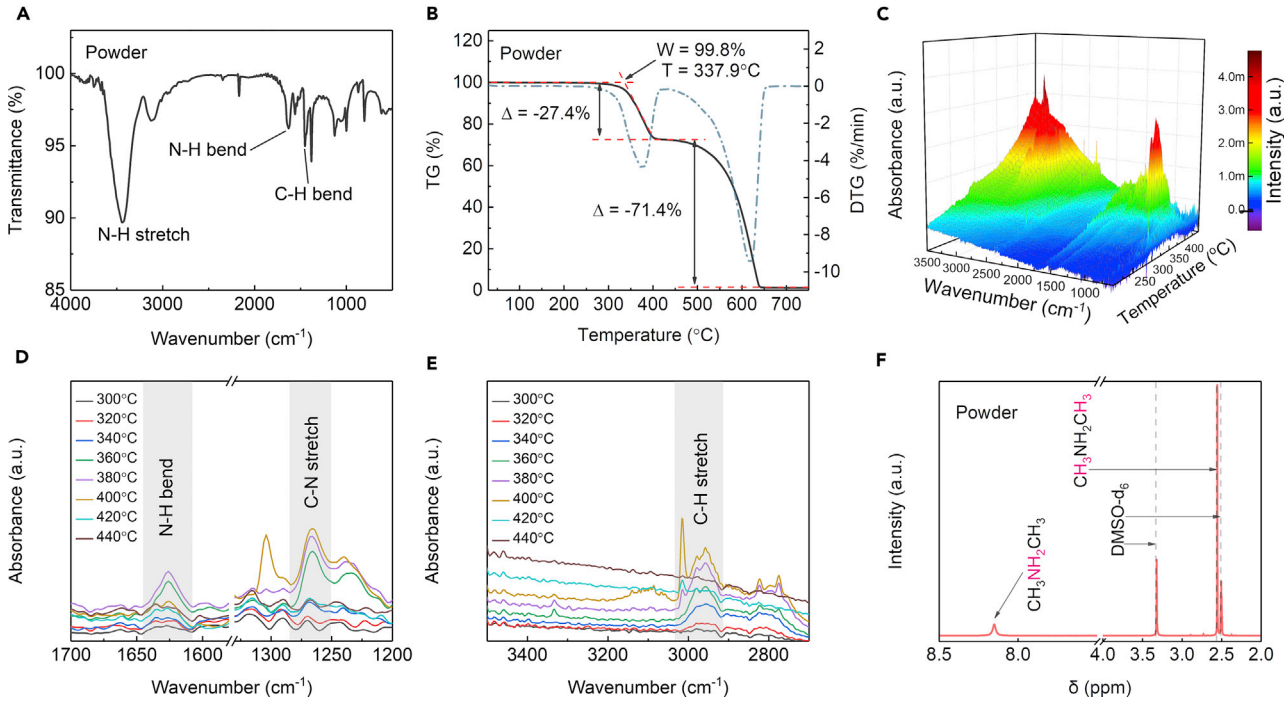

Figure 2. Compositional Analysis of $DMAPbI_3$ Powder

(A) FTIR spectra.

(B) TG-differential TG curve.

(C) Three-dimensional *in situ* TG-FTIR spectra (temperature from 200°C to 440°C).

(D and E) *In situ* TG-FTIR spectra of volatilized products at various temperatures during the thermal degradation. The wavenumber ranges containing (D) N-H bend, C-N stretch and (E) C-H stretch were selected.

(F) ^{1}H NMR spectra; the powder for NMR measurement was dissolved in DMSO-d_6.

(Figures 1E–1H) measurements identify element N uniformly distributed in the entire sample (Figure 1F), together with elements Pb and I (Figures 1G and 1H). The above evidences strongly support that such reaction route in fact produces $DMAPbI_3$; in particular, the universal existence of element N invalidates the misbelief of the delusional "$HPbI_3$" product from this reaction.

We further confirmed the material composition of the $DMAPbI_3$ powder by performing FTIR spectrum, *in situ* TG-FTIR coupled analysis, and ^{1}H NMR measurements. The FTIR spectrum confirms the presence of N-H and C-H bonds (Figure 2A), showing clear signatures of the N-H stretching mode (3,200–3,450 cm^{-1}) and C-H bending mode (1,490–1,350 cm^{-1}) (Jeon et al., 2014). The TG-differential TG data, together with *in situ* TG-FTIR, show two clear weight-losing stages during heat decomposition of the $DMAPbI_3$ powder (Figure 2B). The first stage starts at 337.9°C with 24.7 wt % weight loss, corresponding to the volatilization of organic components, confirmed by the N-H, C-N, and C-H characteristic peaks in the released gases (Figures 2C–2E). During the second decomposition stage (~400°C–640°C), the N-H, C-N, and C-H peaks disappear in the FTIR (Figures 2D and 2E) and the weight loss is consistent with the melting of lead iodide (PbI_2) (bulk melting point at 402°C) (Schieber et al., 2008). In addition, the ^{1}H NMR spectrum (Figure 2F) of the powder (dissolved in dimethyl sulfoxide-d_6, DMSO-d_6) shows clear signals at δ = 8.15 ppm and δ = 2.55 ppm, corresponding to protons in $–NH_2^+–$ and $–CH_3$, respectively (Ke et al., 2018). The integrated ratio from these two signals (corresponding to the molar ratio) is ~1:3, also consistent with the chemical formula DMA^+ ($(CH_3)_2NH_2^+$). All the results again strongly confirm $DMAPbI_3$ as the product from the above reaction, which we will use as the Pb source for fabricating Cs-based perovskites.

We prepared the perovskite precursor solution by dissolving $DMAPbI_3$ powder and CsI in DMF, with a series of CsI/$DMAPbI_3$ molar ratios (CsI from 0.3 to 0.9 M, $DMAPbI_3$ fixed at 1 M, referred to as Cs-0.3, …, Cs-0.9) in the precursor (details in Methods section). A two-step annealing process (140°C + 180°C) was employed to fully crystallize the spin-coated films (Figure 3A), facilitating the formation of $Cs_xDMA_{1-x}PbI_3$ perovskites.

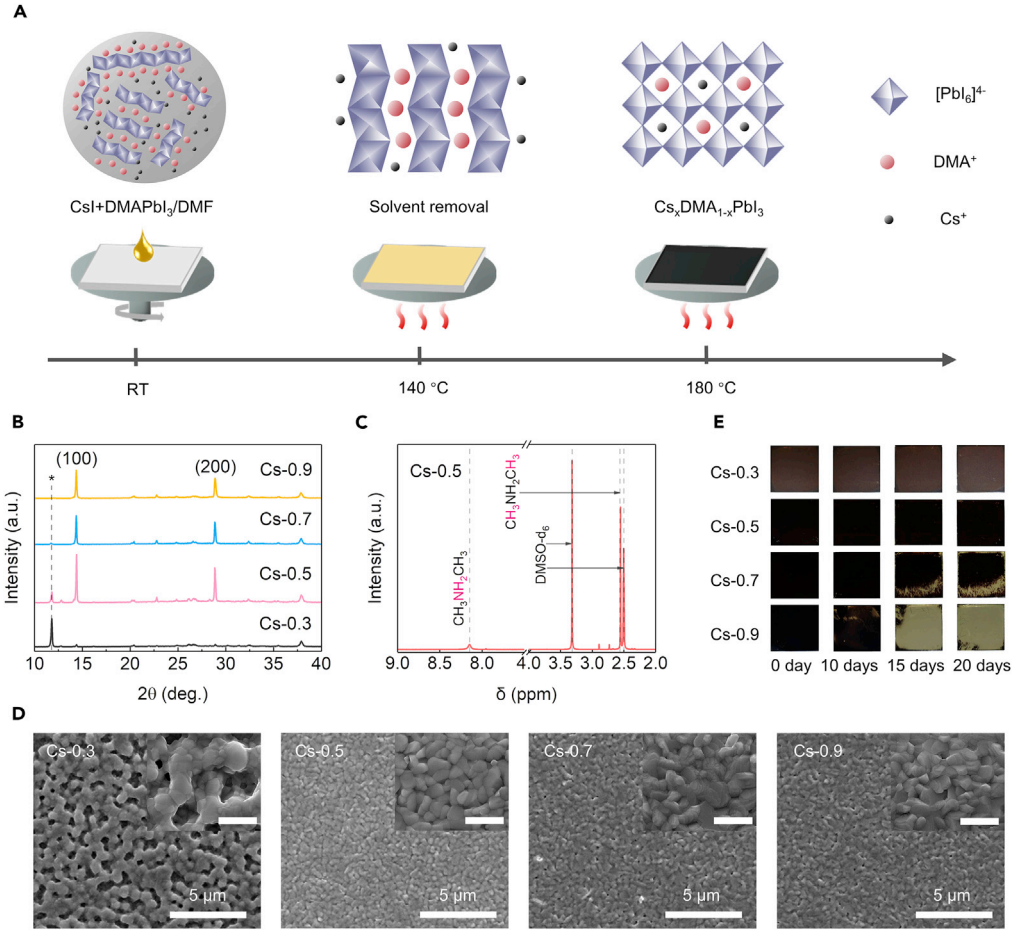

Figure 3. Fabrication and Characterization of $Cs_xDMA_{1-x}PbI_3$ Perovskite Films

(A) Schematic diagram of preparing $Cs_xDMA_{1-x}PbI_3$ perovskite films.

(B) XRD patterns of $Cs_xDMA_{1-x}PbI_3$ films with different molar ratios of CsI/$DMAPbI_3$ in the precursor (Cs-0.9, 0.7, 0.5, and 0.3); peak for $DMAPbI_3$ marked with *; see also Figure S3.

(C) ^{1}H NMR spectra of the powder obtained from scratching the $Cs_xDMA_{1-x}PbI_3$ films when the molar ratio of CsI/$DMAPbI_3$ in the precursor is 0.5/1.

(D) Top-view SEM images of the $Cs_xDMA_{1-x}PbI_3$ films with different concentration of Cs^+; scale bar, 1 μm in insets; see also Figure S5.

(E) Optical photographs of $Cs_xDMA_{1-x}PbI_3$ films with different molar ratio of CsI/$DMAPbI_3$ in ambient condition (RH 20% ± 5%) for 20 days.

The absorption property with different CsI/$DMAPbI_3$ molar ratios was first investigated, showing similar optical features on the spectra (Figure S2). The XRD patterns (Figures 3B and S3) of the obtained films show clear peaks corresponding to $Cs_xDMA_{1-x}PbI_3$ (14.4°, 28.9°) and $DMAPbI_3$ (11.8°), respectively (Ke et al., 2018). Remarkably, in contrast to perovskites fabricated from other conventional routes (such as reacting CsI and PbI_2 with DMAI, Ke et al., 2018, or dissolving CsI and PbI_2 in DMF with HI additive, Zhao et al., 2018), our perovskite films show more intense diffraction peaks of (100) (14.4°) and (200) (28.9°) without any splitting, along with other spurious peaks strongly suppressed. This result suggests that the introduction of DMA^+ (also confirmed by ^{1}H NMR in Figure 3C and FTIR in Figure S4) effectively optimizes tolerance factor, resulting in the high crystallinity and preferable orientation in the perovskite films (Shi et al., 2017).

We noticed that the molar ratio of CsI/$DMAPbI_3$ has clear effects on the resulting $Cs_xDMA_{1-x}PbI_3$ films property. As the Cs^+ ratio increases, the $DMAPbI_3$ XRD peak (2θ = 11.8°) decreases and disappears when the molar ratio is over Cs-0.8. This indicates the existence of excess $DMAPbI_3$ in the perovskite film when CsI molar ratio in the precursor falls below 0.8. SEM images (Figures 3D and S5) show that the Cs-0.5 precursor leads to the optimal film morphology with smooth and dense grains, whereas with

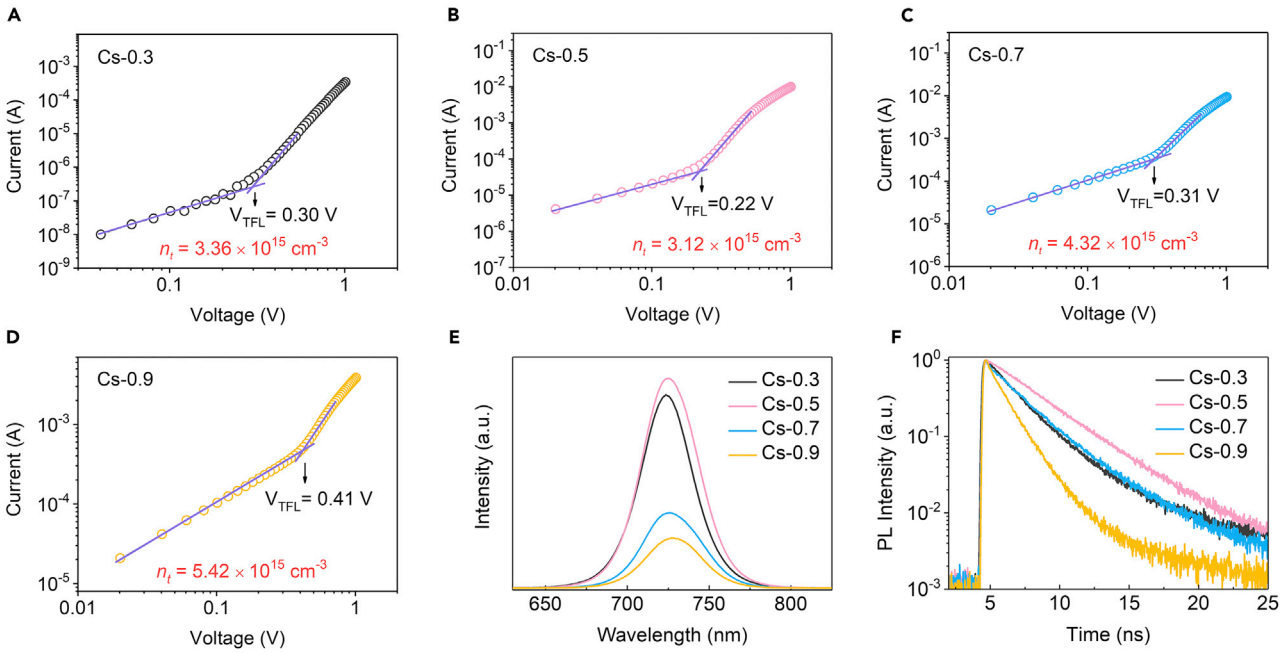

Figure 4. Evaluation of Defect States of $Cs_xDMA_{1-x}PbI_3$ Perovskite films

(A–D) Logarithmic plotted dark *I-V* curves of electron-only devices (FTO/TiO_2/$Cs_xDMA_{1-x}PbI_3$ films/[6,6]-phenyl-C_{61}-butyric acid methyl ester (PCBM)/Au)) based on (A) Cs-0.3, (B) Cs-0.5, (C) Cs-0.7, and (D) Cs-0.9 films; see also Table S1.

(E) PL spectra for $Cs_xDMA_{1-x}PbI_3$ perovskite films.

(F) Time-resolved PL decay trace of $Cs_xDMA_{1-x}PbI_3$ perovskite films; see also Table S2.

insufficient Cs^+ (Cs-0.3) the perovskite film displays many cavities and Cs-0.7, Cs-0.9 films also show emergence of pinholes. We further evaluated the stability of the films processed with different CsI/$DMAPbI_3$ molar ratios. As shown in Figure 3E, the films with low concentrations of Cs^+ (Cs-0.3, Cs-0.5) show negligible degradation after exposing in air for 20 days (relative humidity [RH] 20% ± 5%), whereas those with higher Cs^+ ratio (Cs-0.7, Cs-0.9) quickly degrade from black (α) phase into yellow (δ) phase within a few days (see XRD data in Figure S6). The result suggests that an appropriate ratio of CsI/$DMAPbI_3$ is required for achieving a phase-stable film, which could be attributed to the excess $DMAPbI_3$ in the films acting as a moisture barrier, thus improving the stability of the perovskites.

To understand the effect of the varied CsI/$DMAPbI_3$ molar ratio on the defect property of the $Cs_xDMA_{1-x}PbI_3$ films, we employed the space-charge-limited current method to analyze the electron trap-state density (Figures 4A–4D). The current increases linearly as a function of voltage (indicating Ohmic conduction) up to kink, beyond which the current shows a rapid rise due to the filling of trap states by injected carriers. The voltage at the kink is known as trap-filled limit voltage (V_{TFL}), often used to determine the density of trap states through the equation:

$$V_{TFL} = \frac{en_tL^2}{2\varepsilon\varepsilon_0}$$

where e is the elementary charge, n_t is the density of trap states, L is the film thickness between the two contacts, ε_0 is the vacuum permittivity, and ε is the relative permittivity of $CsPbI_3$ ($\varepsilon = 6.32\varepsilon_0$) (Tong et al., 2016). V_{TFL} and n_t for different Cs^+ concentrations are summarized in Table S1. We noticed that the Cs-0.5 film exhibits lowest density of trap states, which is further evidenced with the strongest luminescence intensity and the longest carrier lifetime from the photoluminescence (PL) and time-resolved PL spectra results, respectively (Figures 4E and 4F). Our results clearly demonstrate the positive effect of engineering the CsI/$DMAPbI_3$ molar ratio on reducing the defect states in the resulting $Cs_xDMA_{1-x}PbI_3$ films.

Having demonstrated the improved stability for films with optimized CsI/$DMAPbI_3$ molar ratio, we further evaluated device efficiency and the stability of resulting complete devices (Figure S7). The PCEs with different ratios are shown in Figures 5A and 5B, and device parameters are summarized in Table S3. The

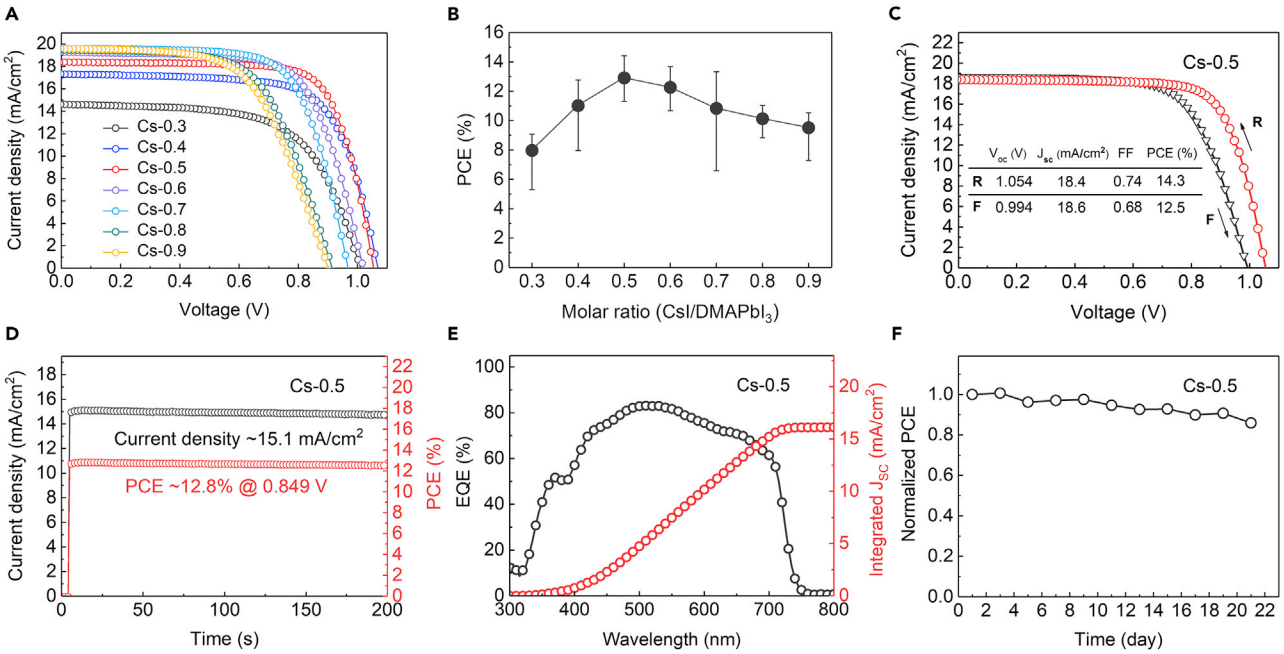

Figure 5. Photovoltaic Performance of $Cs_xDMA_{1-x}PbI_3$ Perovskite Solar Cells

(A) *J-V* curves of the solar cells based on $Cs_xDMA_{1-x}PbI_3$ perovskite films with different compositions (Cs from 0.3 to 0.9); see also Table S3.

(B) PCE of devices with varied $Cs_xDMA_{1-x}PbI_3$ films as a function of the ratio of CsI/$DMAPbI_3$ in the precursor (Cs from 0.3 to 0.9).

(C) *J-V* curves of the champion device (Cs-0.5) in reverse and forward scan directions.

(D) Steady-state PCE and current density of the champion device (Cs-0.5) measured at maximum-power point of 0.849 V.

(E) External quantum efficiency spectra of the best solar cell based on the Cs-0.5 perovskite film.

(F) Evaluation of long-term stability of the device (Cs-0.5) stored in air (RH 20% ± 5%).

optimal composition (i.e., Cs-0.5) yields a champion PCE of 14.3% with a V_{oc} of 1.05 V, a short-circuit current density (J_{sc}) of 18.4 mA/cm^2, and a filling factor of 0.74 (Figure 5C) based on the active layer processed at Cs-0.5, in good agreement with our findings when evaluating the perovskite film quality. We further found that the high performance for Cs-0.5 PSCs was consistent with their high crystal quality and good energy-level alignment at the electron transport interface (Figures S8 and S9). The steady power output for this champion device sustains at 12.8%, measuring at the fixed voltage of 0.849 V close to the maximum power point (Figure 5D), and the external quantum efficiency (EQE) shows an integrated J_{sc} value at 16.1 mA/cm^2 (Figure 5E). We noted that the Cs-0.5 PSCs also exhibit good reproducibility (Figure S10) and good stability, with the best device maintaining 85% of its initial efficiency after 20 days of air exposure (RH 20% ± 5%) without encapsulation (Figure 5F).

Conclusion

In summary, we performed comprehensive characterization of hydrolyzed $DMAPbI_3$ material and systematic evaluation of its effect on fabricating high-quality Cs-based PSCs. Through a series of detailed analysis of the composition and properties of $DMAPbI_3$, including *in situ* TG-FTIR and NMR, we unambiguously determine the existence of $DMAPbI_3$ synthesized from the popular fabrication process—dissolving PbI_2 in DMF with addition of HI—due to the hydrolysis of DMF. By carefully controlling the CsI and $DMAPbI_3$ molar ratio in the precursor, we achieve an optimal composition essential for obtaining high-quality $Cs_xDMA_{1-x}PbI_3$ perovskite films with uniform morphology and low density of trap states, which further leads to optimized $Cs_xDMA_{1-x}PbI_3$ PSCs with highly reproducible PCEs up to 14.3%. Our findings provide an in-depth understanding on the product from hydrolyzed DMF and offer insightful guidelines for achieving high-efficiency stable Cs-based perovskite devices.

Limitation of the Study

In this work, we dissolve PbI_2 and HI in DMF to synthesize $DMAPbI_3$ and confirm that the "mythical" $HPbI_3$ does not exist (which actually should be $DMAPbI_3$) by providing a comprehensive analysis on the

elementary information of the reaction products at every stage. However, the $Cs_xDMA_{1-x}PbI_3$ perovskite film is hard to be stabilized when x is approaching 1 by reacting such $DMAPbI_3$ with CsI. It would be more interesting if the phase transition of $Cs_xDMA_{1-x}PbI_3$ perovskite films was studied through *in situ* measurement, to further investigate the effects of Cs^+/DMA^+ ratio on the phase transition of $Cs_xDMA_{1-x}PbI_3$ perovskites.

METHODS

All methods can be found in the accompanying Transparent Methods supplemental file.

SUPPLEMENTAL INFORMATION

Supplemental Information can be found online at https://doi.org/10.1016/j.isci.2019.04.024.

ACKNOWLEDGMENTS

This work was supported by the National Key R&D Program of China (2017YFA0207400), the National Natural Science Foundation of China (61604032), and the Fundamental Research Funds for the Central Universities in China (ZYGX2016J206).

AUTHOR CONTRIBUTIONS

M.L. conceived the idea of the work. Y.P. and S.B. proposed the experimental design. Y.L. synthesized and characterized the $DMAPbI_3$ powder. Y.P. and F.L. performed the device fabrication and corresponding characterization. X.J. performed *in situ* TG-FTIR. All authors contributed to the manuscript.

DECLARATION OF INTERESTS

The authors declare no competing interests.

Received: January 28, 2019
Revised: April 12, 2019
Accepted: April 18, 2019
Published: May 31, 2019

REFERENCES

Daub, M., and Hillebrecht, H. (2018). On the demystification of "$HPbI_3$" and the peculiarities of the non-innocent solvents H_2O and DMF. Z. Anorg. Allg. Chem. *644*, 1393–1400.

Eperon, G.E., Paterno, G.M., Sutton, R.J., Zampetti, A., Haghighirad, A.A., Cacialli, F., and Snaith, H.J. (2015). Inorganic caesium lead iodide perovskite solar cells. J. Mater. Chem. A *3*, 19688–19695.

Fu, Y., Rea, M.T., Chen, J., Morrow, D.J., Hautzinger, M.P., Zhao, Y., Pan, D., Manger, L.H., Wright, J.C., Goldsmith, R.H., et al. (2017). Selective stabilization and photophysical properties of metastable perovskite polymorphs of $CsPbI_3$ in thin films. Chem. Mater. *29*, 8385–8394.

Hu, Y., Bai, F., Liu, X., Ji, Q., Miao, X., Qiu, T., and Zhang, S. (2017). Bismuth incorporation stabilized α-$CsPbI_3$ for fully inorganic perovskite solar cells. ACS Energy Lett. *2*, 2219–2227.

Jena, A.K., Kulkarni, A., Sanehira, Y., Ikegami, M., and Miyasaka, T. (2018). Stabilization of α-$CsPbI_3$ in ambient room temperature conditions by incorporating Eu into $CsPbI_3$. Chem. Mater. *30*, 6668–6674.

Jeon, N.J., Noh, J.H., Kim, Y.C., Yang, W.S., Ryu, S., and Seok, S.I. (2014). Solvent engineering for high-performance inorganic–organic hybrid perovskite solar cells. Nat. Mater. *13*, 897–903.

Ju, D., Zhao, T., Yangyang, D., Zhang, G., Hu, X., Cui, D., and Tao, X. (2017). Gas induced conversion of hybrid perovskite single crystal to single crystal for great enhancement of their photoelectric properties. J. Mater. Chem. A *5*, 21919–21925.

Ke, W., Spanopoulos, I., Stoumpos, C.C., and Kanatzidis, M.G. (2018). Myths and reality of $HPbI_3$ in halide perovskite solar cells. Nat. Commun. *9*, 4785.

Lau, C.F.J., Deng, X., Zheng, J., Kim, J., Zhang, Z., Zhang, M., Bing, J., Wilkinson, B., Hu, L., Patterson, R., et al. (2018). Enhanced performance via partial lead replacement with calcium for a $CsPbI_3$ perovskite solar cell exceeding 13% power conversion efficiency. J. Mater. Chem. A *6*, 5580–5586.

Li, B., Zhang, Y., Fu, L., Yu, T., Zhou, S., Zhang, L., and Yin, L. (2018a). Surface passivation engineering strategy to fully-inorganic cubic $CsPbI_3$ perovskites for high-performance solar cells. Nat. Commun. *9*, 1076.

Li, F., Pei, Y., Xiao, F., Zeng, T., Yang, Z., Xu, J., Sun, J., Peng, B., and Liu, M. (2018b). Tailored dimensionality to regulate the phase stability of inorganic cesium lead iodide perovskites. Nanoscale *10*, 6318–6322.

Liao, J., Rao, H., Chen, B., Kuang, D., and Su, C. (2017). Dimension engineering on cesium lead iodide for efficient and stable perovskite solar cells. J. Mater. Chem. A *5*, 2066–2072.

Long, M., Zhang, T., Chai, Y., Ng, C.-F., Mak, T.C.W., Xu, J., and Yan, K. (2016). Nonstoichiometric acid–base reaction as reliable synthetic route to highly stable $CH_3NH_3PbI_3$ perovskite film. Nat. Commun. *7*, 13503.

Luo, P., Xia, W., Zhou, S., Sun, L., Cheng, J., Xu, C., and Lu, Y. (2016). Solvent engineering for ambient-air-processed, phase-stable $CsPbI_3$ in perovskite solar cells. J. Phys. Chem. Lett. *7*, 3603–3608.

Mancini, A., Quadrelli, P., Amoroso, G., Milanese, C., Boiocchi, M., Sironi, A., Patrini, M., Guizzetti, G., and Malavasi, L. (2016). Synthesis, structural and optical characterization of $APbX_3$ (A=methylammonium, dimethylammonium, trimethylammonium, X=I, Br, Cl) hybrid organic-inorganic materials. J. Solid State Chem. *240*, 55–60.

Noel, N.K., Congiu, M., Ramadan, A.J., Fearn, S., McMeekin, D.P., Patel, J.B., Johnston, M.B., Wenger, B., and Snaith, H.J. (2017). Unveiling the

influence of pH on the crystallization of hybrid perovskites, delivering low voltage loss photovoltaics. Joule *1*, 328–343.

Pang, S., Zhou, Y., Wang, Z., Yang, M., Krause, A.R., Zhou, Z., Zhu, K., Padture, N.P., and Cui, G. (2016). Transformative evolution of organolead triiodide perovskite thin films from strong room-temperature solid-gas interaction between $HPbI_3$-CH_3NH_2 precursor pair. J. Am. Chem. Soc. *138*, 750–753.

Sanehira, E.M., Marshall, A.R., Christians, J.A., Harvey, S.P., Ciesielski, P.N., Wheeler, L.M., Schulz, P., Lin, L.Y., Beard, M.C., and Luther, J.M. (2017). Enhanced mobility $CsPbI_3$ quantum dot arrays for record-efficiency, high-voltage photovoltaic cells. Sci. Adv. *3*, eaao4204.

Schieber, M., Zamoshchik, N., Khakhan, O., and Zuck, A. (2008). Structural changes during vapor-phase deposition of polycrystalline-PbI_2 films. J. Cryst. Growth *310*, 3168–3173.

Shi, Z., Zhang, Y., Cui, C., Li, B., Zhou, W., Ning, Z., and Mi, Q. (2017). Symmetrization of the crystal lattice of $MAPbI_3$ boosts the performance and stability of metal–perovskite photodiodes. Adv. Mater. *29*, 1701656.

Sutherland, B.R. (2017). Perovskite precursors get a pH tune-up. Joule *1*, 221–223.

Swarnkar, A., Marshall, A.R., Sanehira, E.M., Chernomordik, B.D., Moore, D.T., Christians, J.A., Chakrabarti, T., and Luther, J.M. (2016). Quantum dot-induced phase stabilization of α-$CsPbI_3$ perovskite for high-efficiency photovoltaics. Science *354*, 92–95.

Tong, Y., Bladt, E., Ayguler, M.F., Manzi, A., Milowska, K.Z., Hintermayr, V.A., Docampo, P., Bals, S., Urban, A.S., Polavarapu, L., et al. (2016). Highly luminescent cesium lead halide perovskite nanocrystals with tunable composition and thickness by ultrasonication. Angew. Chem. Int. Ed. *55*, 13887–13892.

Wang, F., Yu, H., Xu, H., and Zhao, N. (2015). $HPbI_3$: a new precursor compound for highly efficient solution-processed perovskite solar cells. Adv. Funct. Mater. *25*, 1120–1126.

Wang, Q., Zheng, X., Deng, Y., Zhao, J., Chen, Z., and Huang, J. (2017). Stabilizing the α-phase of $CsPbI_3$ perovskite by sulfobetaine zwitterions in one-step spin-coating films. Joule *1*, 371–382.

Wang, K., Jin, Z., Liang, L., Bian, H., Bai, D., Wang, H., Zhang, J., Wang, Q., and Liu, S. (2018a). All-inorganic cesium lead iodide perovskite solar cells with stabilized efficiency beyond 15%. Nat. Commun. *9*, 4544.

Wang, P., Zhang, X., Zhou, Y., Jiang, Q., Ye, Q., Chu, Z., Li, X., Yang, X., Yin, Z., and You, J. (2018b). Solvent-controlled growth of inorganic perovskite films in dry environment for efficient and stable solar cells. Nat. Commun. *9*, 2225.

Wang, Y., Zhang, T., Kan, M., Li, Y., Wang, T., and Zhao, Y. (2018c). Efficient α-$CsPbI_3$ photovoltaics with surface terminated organic cations. Joule *2*, 2065–2075.

Wang, Y., Zhang, T., Kan, M., and Zhao, Y. (2018d). Bifunctional Stabilization of All-inorganic α-$CsPbI_3$ perovskite for 17% efficiency photovoltaics. J. Am. Chem. Soc. *140*, 12345–12348.

Zhang, T., Dar, M.I., Li, G., Xu, F., Guo, N., Gratzel, M., and Zhao, Y. (2017). Bication lead iodide 2D perovskite component to stabilize inorganic α-$CsPbI_3$ perovskite phase for high-efficiency solar cells. Sci. Adv. *3*, e1700841.

Zhao, B., Jin, S., Huang, S., Liu, N., Ma, J., Xue, D., Han, Q., Ding, J., Ge, Q., Feng, Y., et al. (2018). Thermodynamically stable orthorhombic γ-$CsPbI_3$ thin films for high-performance photovoltaics. J. Am. Chem. Soc. *140*, 11716–11725.

ISCI, Volume *15*

Supplemental Information

Unveiling Property of Hydrolysis-Derived $DMAPbI_3$ for Perovskite Devices: Composition Engineering, Defect Mitigation, and Stability Optimization

Yunhe Pei, Yang Liu, Faming Li, Sai Bai, Xian Jian, and Mingzhen Liu

Supplemental Information

This PDF file includes:

Figures S1 to S10

Tables S1 to S3

Transparent Methods

Figures:

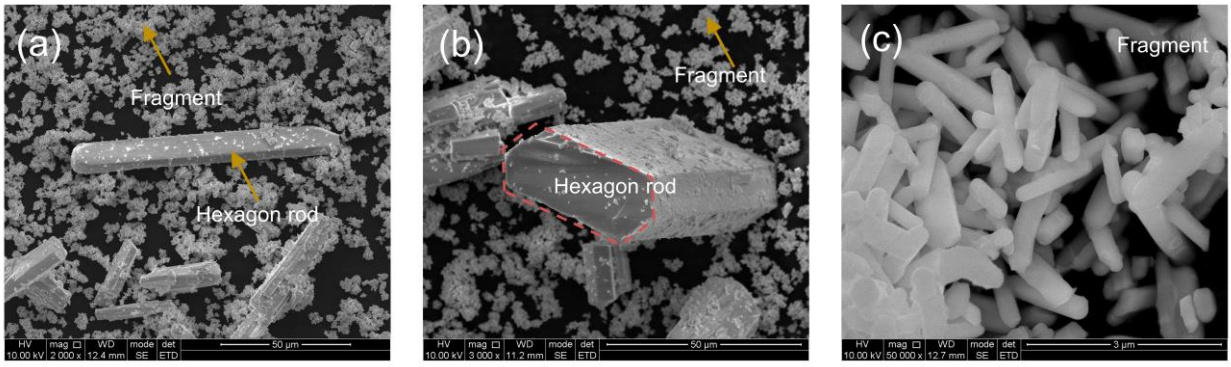

Figure S1. SEM images of lead source powder, Related to Figure 1.

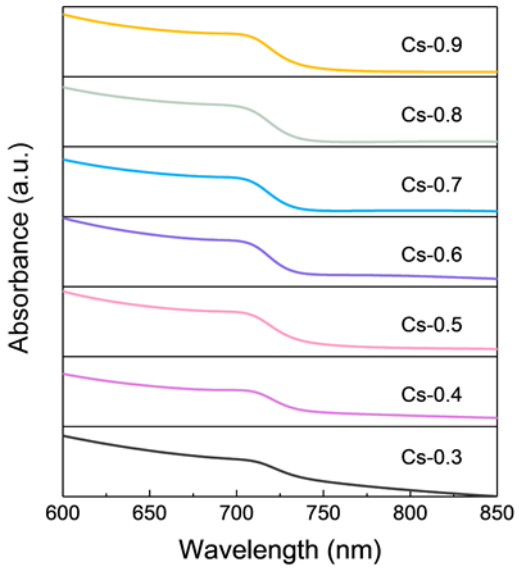

Figure S2. UV-vis spectra of perovskite films, Related to Figure 3.

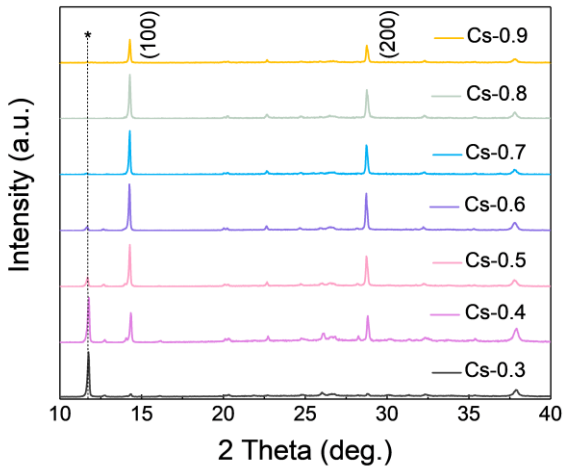

Figure S3. XRD pattern of $Cs_xDMA_{1-x}PbI_3$ perovskites, Peak for $DMAPbI_3$ marked with '*', Related to Figure 3B.

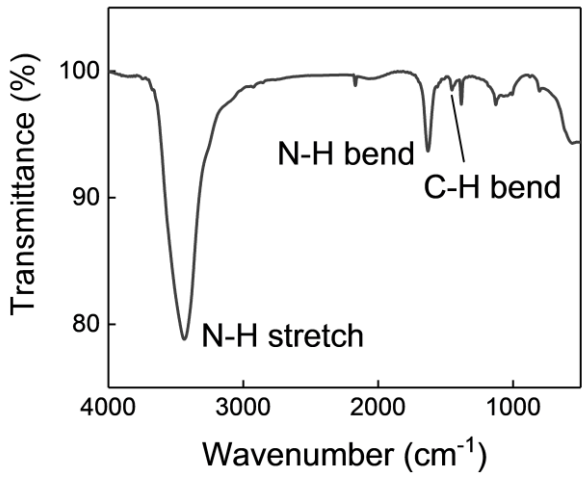

Figure S4. FTIR of powder obtained from scratching away the $Cs_xDMA_{1-x}PbI_3$ film (Cs-0.5), Related to Figure 3.

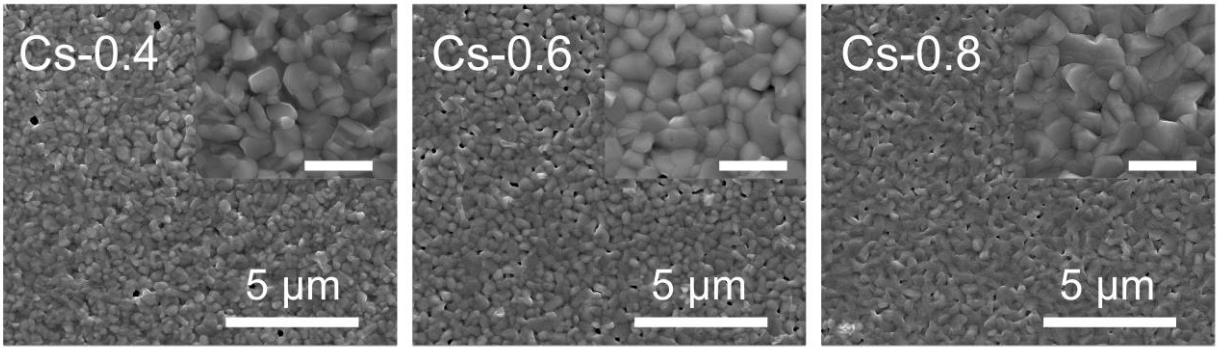

Figure S5. Top view SEM images of perovskite films with different CsI/DMAPbI$_3$ molar ratio, Related to Figure 3D. scale bar is 1 μm in inserted images.

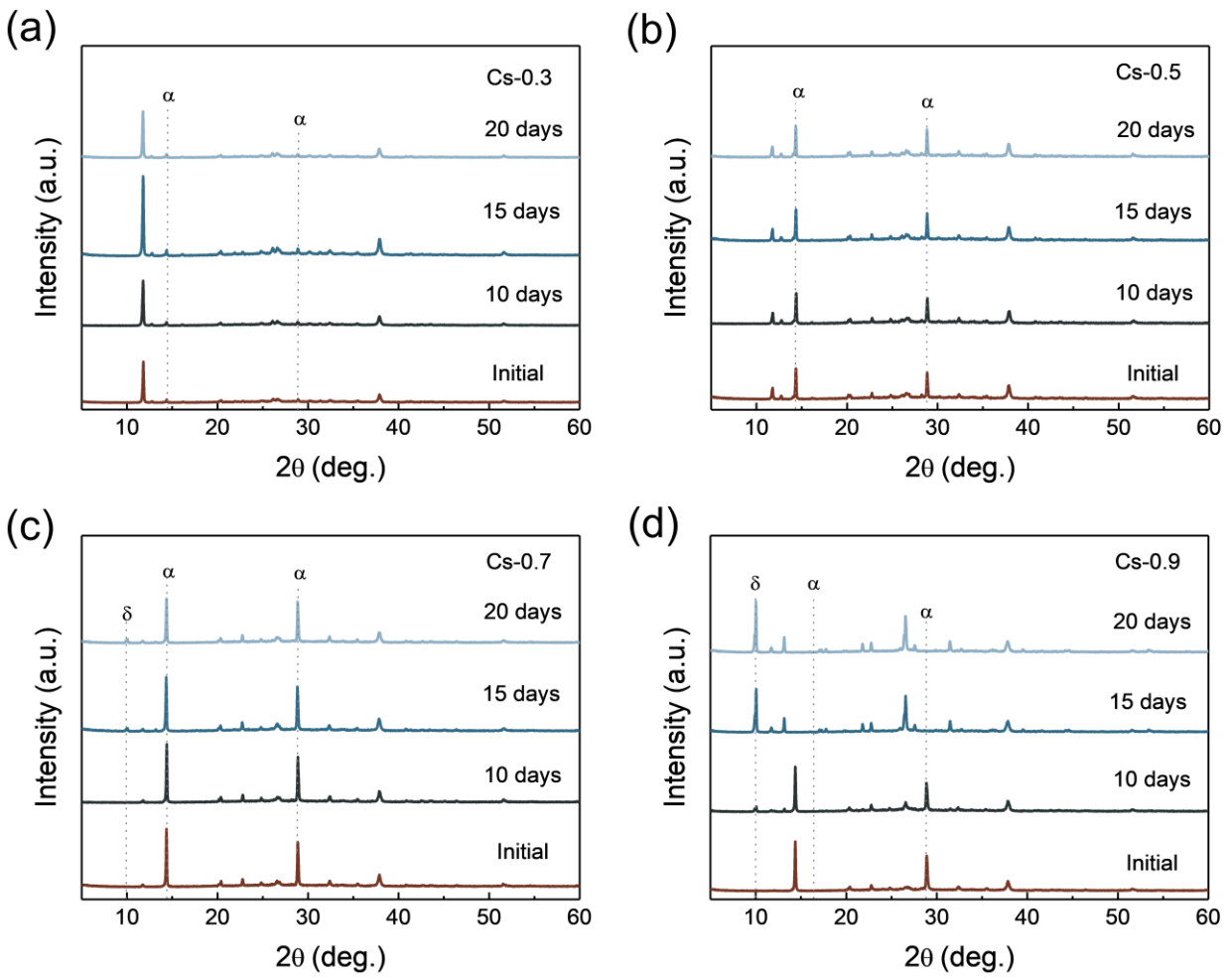

Figure S6. Characterization of perovskite films under humid environment (20±5%). The structural evolution of (a) Cs-0.3 film, (b) Cs-0.5 film, (c) Cs-0.7 film and (d) Cs-0.9 film, Related to Figure 3E.

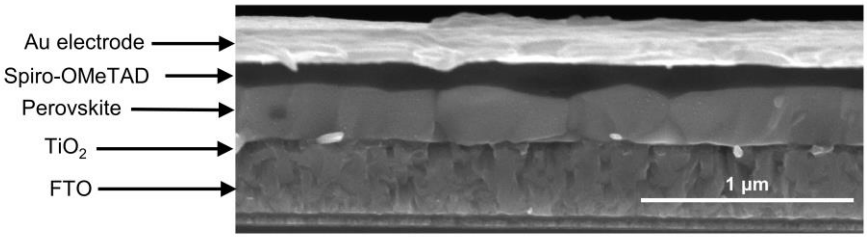

Figure S7. Cross view SEM image of $Cs_xDMA_{1-x}PbI_3$ perovskite solar cells, Related to Figure 5.

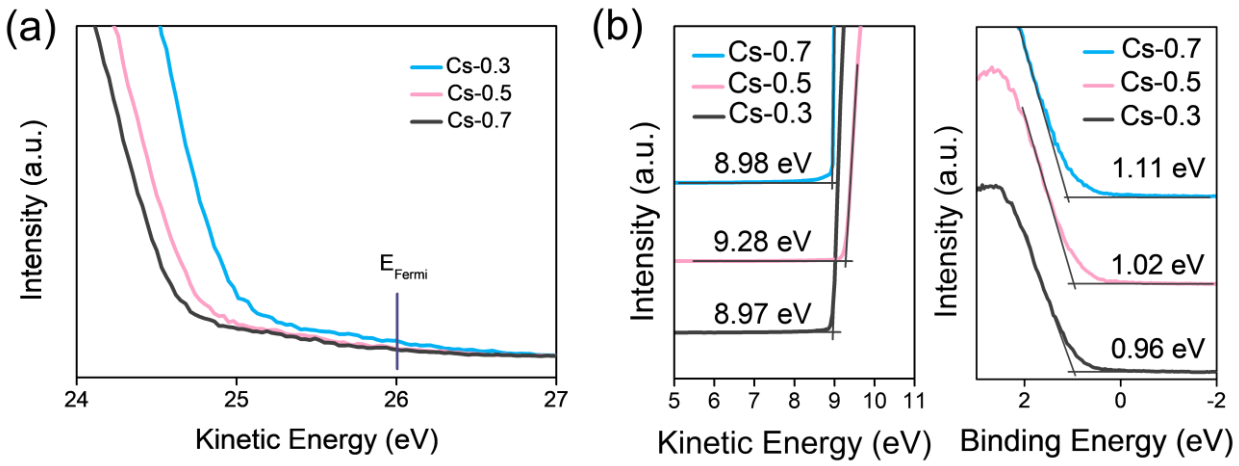

Figure S8. (a) Fermi edge region for perovskite films. (b) UPS cut-off region (left) and VB region (right) of perovskite films. A bias voltage of -5 V was applied. The work function (W_F) can be calculated according to $h\nu$-W_F =E_{Fermi} -E_{cutoff}. The W_F can be calculated to 4.17 eV (Cs-0.3), 4.48 eV (Cs-0.5) and 4.18 eV (Cs-0.7), respectively. Related to Figure 5.

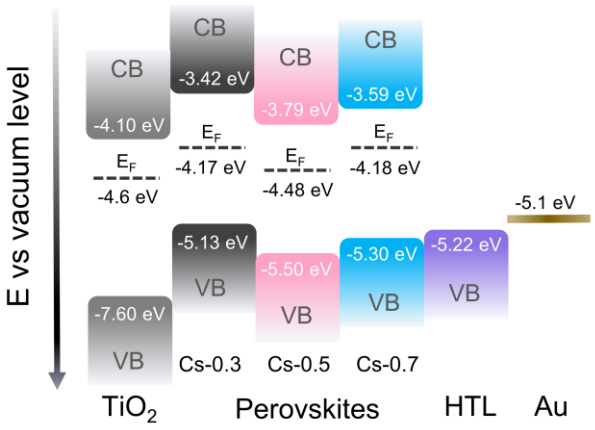

Figure S9. Diagram of energy level of perovskite films, Related to Figure 5.

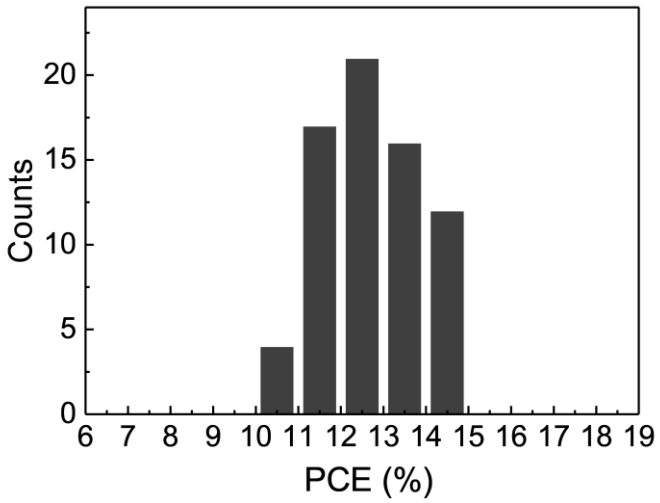

Figure S10. PCE histograms for solar cells based on Cs-0.5 perovskite film, Related to Figure 5.

Tables:

Table S1. Electron trap-state density of $Cs_xDMA_{1-x}PbI_3$ perovskite films, Related to Figure 4 A-D.

CsI/DMAPbI$_3$ molar ratio in precursor	0.3	0.5	0.7	0.9
V_{TFL} (V)	0.30	0.22	0.31	0.41
Trap-state density (cm^{-3})	3.36×10^{15}	3.12×10^{15}	4.32×10^{15}	5.42×10^{15}

Table S2. The fitted PL lifetime of perovskite films, Related to Figure 4F.

Sample	A_1	t_1(ns)	A_2	t_2(ns)	t_{ave} (ns)
Cs-0.3	0.97%	8.2	99.03%	2.1	2.16
Cs-0.5	61.29%	3.5	38.71%	3.5	3.50
Cs-0.7	78.30%	1.8	21.70%	3.4	2.15
Cs-0.9	4.11%	1.5	95.89%	0.6	0.64

Table S3. PV parameters of optimized devices based on various perovskites, Related to Figure 5A.

CsI/DMAPbI$_3$ molar ratio in precursor	0.3	0.4	0.5	0.6	0.7	0.8	0.9
J_{sc} (mA/cm^2)	14.6	17.3	18.4	19.3	19.6	19.5	19.6
V_{oc} (V)	1.009	1.068	1.054	1.019	0.967	0.912	0.899
PCE (%)	9.3	12.9	14.3	13.5	13.1	11.0	10.5
FF	0.63	0.70	0.74	0.69	0.69	0.62	0.60

Transparent Methods

Materials: Hydroiodic acid (HI, Alfa, 57 wt% in H_2O), PbI_2 (99.9%, Sigma-Aldrich), CsI (>99.99%, Xi'an Polymer Light Technology Corp.), lithium bis(trifluoromethanesulfonyl)imide (Li-TFSI, 99.95%, Sigma-Aldrich), 4-tert-butylpyridine (4-tBP, 96%, Sigma-Aldrich), chlorobenzene (Sigma-Aldrich), *N,N*-dimethyiformamide (DMF, 99.8%, Sigma-Aldrich) and all other chemicals were all used as received without further purification. TiO_2 sol (ethanol solution containing a 10% volume fraction of tetrabutyl titanate) was synthesized.

***Preparation of $DMAPbI_3$ powder*:** $DMAPbI_3$ precursor was prepared by dissolving PbI_2 (4.62 g) in DMF (10 mL) and then adding HI (3.6 mL), followed by stirring at 50°C overnight to ensure complete reaction. In order to remove excess HI, the precursor was then washed in absolute ethanol to obtain the light-yellow precipitate. Particularly, the amount of ethanol plays a key role in the synthesis of high quality $DMAPbI_3$ powder. The heating temperature during stirring should be controlled accurately. The obtained powder was dried in vacuum at 65°C for 12 h and stored in a nitrogen glovebox.

***Preparation of $Cs_xDMA_{1-x}PbI_3$ films*:** CsI and $DMAPbI_3$ powder in different molar ratios (CsI from 0.3 M to 0.9 M, $DMAPbI_3$ fixed at 1 M) were dissolved in 1 mL DMF, followed by stirring for 40 min at room temperature (RT). The perovskite films for characterization were formed through spin-coating 70 μL perovskite precursor onto the FTO substrate or the compact TiO_2 substrate at 4000 rpm for 30 s and then annealing at 140 °C for 2 min and 180 °C for 4 min. The transfer of temperature should be finished quickly.

***Device fabrication*:** The device fabrication was conducted based on FTO substrates which were cleaned with deionized water, acetone and ethanol in ultrasonic cleaner. Then FTO substrates were treated in O_2 plasma cleaner for 10 min. For the formation of compact TiO_2 layer, TiO_2 precursor sol was spun-coated on the substrates at 3000 rpm for 30 s, followed by annealing at 500 °C for 30 min in air. The compact TiO_2 coated substrates were then treated with UV-ozone for 10 min. Subsequently, the perovskite layer was deposited via spin-coating. The spiro-OMeTAD precursor was prepared by dissolving 80 mg spiro-OMeTAD with 35 μL LiTFSI solution (520 mg in 1 mL acetonitrile) and 28.8 μl 4-tBP in 1 mL chlorobenzene. Hole transport layer was deposited on top of perovskite film by spin-coating at 4000 rpm for 40 s. Finally, a ~100 nm Au electrode was deposited by thermal evaporation under the pressure of 5×10^{-4} Pa.

***Measurements and Characterization*:** X-ray diffraction (XRD) patterns of films and powder were recorded by a Bruker D8 Advance diffractometer with Cu K_α radiation (λ = 1.5418 Å) and LYNXEYE_XE detector. Scanning electron microscope (SEM) images were collected by FEI Inspect F50 electron microscope with electron energy of 10 keV. The energy disperse spectroscopy analysis (EDS) was also performed on FEI Inspect F50. Steady-state photoluminescence (PL) measurements and time-resolved PL decay were conducted by using FluoTime 300 (PicoQuant). The *J-V* curves were measured by Keithley 2400 series digital source-meter unit and the devices were placed under simulated AM 1.5G irradiation (100 mW/cm^2, xenon lamp, Newport). The effective area of one cell is 0.09 cm^2. Ultraviolet photoelectron spectra (UPS) were carried out by Thermo Fisher Scientific Escalab 250Xi system by using a He discharge lamp (21.22 eV), a bias voltage of -5 V was applied. X-ray photoelectron spectroscopy (XPS) was performed by the same system as UPS. Fourier transform infrared (FTIR) spectra were measured by the Thermo Scientific Nicolet IS 10 FTIR spectrometer. Nuclear magnetic resonance (^{1}H NMR) spectra were measured with Bruker Advance 400 spectrometer. The space-charge-limited current (SCLC) measurements were carried out by Keithley 2400 digital source-meter under dark condition. The external quantum efficiency (EQE) spectra were measured using a QTEST HIFINITY 5 (Crowntech Inc., USA). Thermogravimetry *in situ* infrared spectroscopy (TG-FTIR) coupled analysis was performed on PerkinElmer STA8000 simultaneous thermal analyzer combined with Frontier FTIR. The heating rate is 10 K/min.